Research Article

International Journal of Advanced Technology and Engineering Exploration, Vol 12(131)
ISSN (Print): 2394-5443 ISSN (Online): 2394-7454
http://dx.doi.org/10.19101/IJATEE.2024.111100951

Deep learning–based classification of brain tumors from MRI images

N. Kopperundevi[1*], V. Lakshmi Praba[2], S. Senthilkumar[3], V. Mohan[4] and Dhinesh Vijayakumar[5]
School of Computer Science and Engineering, Vellore Institute of Technology, Vellore, 632014, Tamil Nadu, India[1]
Department of Electronics and Communication Engineering, E.G.S. Pillay Engineering College, Nagapattinam, 611002, Tamil Nadu, India[2]
Department of Electronics and Communication Engineering, E.G.S. Pillay Engineering College, Nagapattinam, 611002, Tamil Nadu, India[3]
Department of Electrical and Electronics Engineering, E.G.S. Pillay Engineering College, Nagapattinam, 611002, Tamil Nadu, India[4]
APM and Data Analytics Lead, TMX, Toronto, Canada[5]

Received: 02-June-2024; Revised: 04-October-2025; Accepted: 14-October-2025

Abstract
The inherent complexity of brain tumor morphology and the variability among different tumor types present significant challenges for accurate classification. Traditional imaging analysis methods often fail to fully exploit the rich information available in magnetic resonance imaging (MRI), resulting in a critical research gap in developing automated and reliable tumor classification systems. This study introduces a novel deep learning model designed to improve the accuracy of brain tumor classification using only MRI brain images. The proposed model employs an advanced convolutional neural network (ACNN) architecture optimized for medical imaging, capable of capturing intricate patterns and features characteristic of specific tumor types. Multimodal brain tumor segmentation (BraTS2020) dataset has been used for experimentation. The collected data undergo pre-processing using the adaptive fuzzy filtering (AFF) method. Segmented images are then derived from these pre-processed images through wavelet transformation. From these segmented images, features are extracted using texture analysis techniques. These extracted features are subsequently classified using the proposed ACNN, where the network parameters are optimized through the nature-inspired artificial hummingbird algorithm (AHA), with accuracy maximization, which is serving as the primary fitness function. The optimized ACNN model classifies the final output into three categories: benign, pre-malignant, and malignant tumors. To evaluate the model's performance, comprehensive metrics such as accuracy, precision, recall, and F1-score are employed for a thorough assessment. This approach effectively bridges the gap in automated brain tumor classification and provides a robust tool to support healthcare professionals in diagnosis and treatment planning. Overall, the study emphasizes the growing importance of MRI in medical imaging and showcases recent advancements in deep learning–based techniques for brain tumor analysis.

Keywords
Brain tumor classification, Magnetic resonance imaging, Deep learning, Convolutional neural network, Artificial hummingbird algorithm, Medical image analysis.

1.Introduction
Brain tumors are abnormal growths within the brain or central spinal canal, significantly impacting neurological functions and potentially leading to life-threatening conditions. Globally, an approximate of 300,000 new cases is diagnosed every year, highlighting the urgency of effective diagnostic tools [1].

Magnetic resonance imaging (MRI) is a standard modality for brain tumor diagnosis due to its ability to provide detailed visualization of soft tissues [2]. However, manual interpretation of MRI scans by radiologists is often subjective, time-consuming, and prone to inter-observer variability [3]. Early computational methods relying on handcrafted features and traditional machine learning have shown limited success due to their dependence on feature selection and lack of generalization across datasets [4, 5]. Recent advancements in deep learning, particularly convolutional neural networks (CNNs),

*Author for correspondence

have demonstrated remarkable capabilities in automating feature extraction and improving classification accuracy in medical imaging [6–8]. These models outperform traditional methods by leveraging hierarchical feature learning to identify complex patterns in MRI data [9]. Nevertheless, the integration of optimization algorithms with CNN architectures has emerged as a promising approach to further enhance classification efficiency [10]. *Figure 1* depicts a clear distinction between normal and tumor MRI scans of the brain.

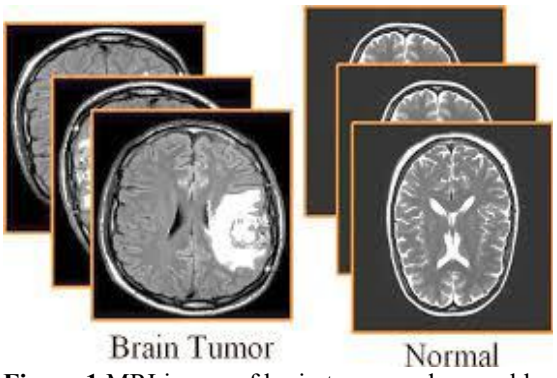

Figure 1 MRI image of brain tumor and normal brain images

Classifying brain tumors from MRI scans is challenging due to the variability in tumor morphology, overlap in visual characteristics between tumor types, and the presence of imaging artifacts [11]. Traditional CNNs face limitations such as high computational overhead, sensitivity to parameter tuning, and prolonged training times [12]. Additionally, segmentation methods often fail to capture intricate textural and morphological features accurately [13]. This study addresses these challenges by proposing a novel Advanced CNN (ACNN) optimized using the artificial hummingbird algorithm (AHA) to enhance classification accuracy and efficiency [14, 15].

This paper aims to develop a robust deep learning framework for classifying brain tumors using MRI scans, integrating advanced CNN architectures with the AHA optimization algorithm to achieve high accuracy, efficiency and reliability.

The study introduces a novel CNN architecture customized for medical imaging, leveraging the AHA for optimal parameter tuning. The key contributions include:

1. Development of a pre-processing pipeline using adaptive fuzzy filtering (AFF) for enhanced image quality.
2. Integration of wavelet transformation for precise segmentation and texture analysis for feature extraction.
3. Demonstration of significant performance improvements in classification accuracy, precision, recall, and F1-score over existing methods.

Accurate identification of tumor types is a crucial first stage in the clinical diagnosis process and subsequent successful patient evaluation. MRI represents the most commonly used technique for tumor-type differential diagnosis [16–19]. However, it's interpretation is subject to human variability, making it challenging to process a large amount of information. The radiologist's experience plays a major role in the early diagnosis of brain tumors. The diagnostic process cannot be completed before determining whether the tumor is malignant or benign. Typically, a biopsy is done to determine if the tissue is benign or cancerous. The biopsy associated with a brain tumor is typically not performed before the final brain surgery, in contrast to tumors located elsewhere in the body. It is crucial to provide an efficient diagnostic platform for both tumor segmentation as well as classification from MRI scans to achieve accurate diagnoses, preventing unnecessary surgery, and reducing subjectivity [20]. The medical sector has been greatly impacted by advancement in novel methodologies, particularly deep learning, and artificial intelligence (AI), which have become vital support systems for many medical specialties, including imaging. Several deep-learning techniques for image segmentation and classification are used in MRI image processing to provide radiologists with a second opinion.

This research work introduces several unique contributions to the domain of brain tumor classification using MRI scans. The primary novelty lies in the development of the ACNN, specifically optimized for medical imaging tasks, integrated with the AHA for hyperparameter tuning. Unlike existing models that use fixed or heuristic parameter settings, the AHA-enabled ACNN dynamically adapts its parameters to maximize classification accuracy, thereby enhancing the model's robustness and generalization. Another significant contribution is the tailored preprocessing pipeline that employs AFF for noise reduction while preserving critical tumor textures. The use of AFF ensures high-quality input data, improving the effectiveness of subsequent

segmentation and classification steps. Furthermore, the use of wavelet transformation for segmentation represents a strategic choice, enabling precise isolation of tumor regions through multi-scale analysis, which is particularly suited for complex medical imaging datasets. Lastly, the comprehensive evaluation of the proposed framework against state-of-the-art models demonstrates its superiority in terms of accuracy, precision, recall, and F1-score. The framework not only achieves higher performance metrics but also provides a robust and efficient solution for brain tumor classification, paving the way for future research on integrating nature-inspired optimization techniques with advanced deep learning models in medical imaging.

The paper is structured as follows: Section 2 presents a literature survey. Section 3 describes the proposed methodology. Section 4 discusses experimental results. Section 5 concludes the study and highlights future research directions.

2.Related work

This section provides a detailed review on the different deep learning methods such as generative adversarial network (GAN), CNN, YOLOv8, etc. in the literature to classify the brain tumors using MRI images.

Marina [21] proposed a GAN-CNN hybrid framework for brain tumor classification, using GANs to address dataset scarcity and CNNs for multi-class classification. The model achieved up to 99% accuracy with strong generalization. However, reliance on synthetic data and high computational costs limit its real-time clinical use. Khan et al. [22] developed a diagnostic system using pre-processing (Gaussian filtering, skull stripping), grey-level co-occurrence matrix (GLCM) based features, and CNN/long short-term memory (LSTM) models, achieving 84.5% accuracy with CNN. The method reduces invasive diagnoses but has moderate accuracy compared to newer deep models and depends heavily on pre-processing.

Jader et al. [23] introduced an ensemble framework combining VGG-16, residual neural network-50 (ResNet-50), and AlexNet via transfer learning, reporting 99.16% accuracy and high precision/recall. The approach outperformed traditional methods and reduced the dependency of radiologist, but reliance on pre-trained models and high computational demand remain limitations. Owida et al. [24] used EfficientNetB3 with batch normalization, dropout, and dense regularization on 7,023 MRI images achieving 100% accuracy. The model shows strong clinical potential but suffers from limited dataset diversity, requiring validation on multi-institutional datasets.

Bhimavarapu et al. [25] combined improved fuzzy c-means (FCM) segmentation with an enhanced Extreme Learning Machine classifier achieving up to 99.37% accuracy. The method detects small tumors effectively, but faces computational complexity and sensitivity to artefacts, limiting generalization. Zebari et al. [26] proposed a fusion model integrating ResNet50 and convolutional deep belief networks (CDBN) with data augmentation, achieving 98.98% accuracy. The approach captures local and global features, but depends on augmented datasets and has high computational complexity for clinical use.

Karimullah et al. [27] integrated harmony search optimization with CNN for brain tumor detection, achieving 99.13% accuracy. The method enhances robustness and feature selection, but introduces computational overhead and requires large, high-quality datasets. Alqhtani et al. [28] combined contrast-limited adaptive histogram equalization (CLAHE), diffusion filtering, FCM clustering, and support vector machine (SVM) for CE-MRI tumor classification, achieving accuracy of 0.982 with fast 0.42s processing. Despite efficiency, generalization is limited by dataset dependency and sensitivity to parameter tuning.

Elgohr et al. [29] applied YOLOv8 for real-time brain tumor detection, reaching 96% training and 100% testing accuracy. The model captures well the spatial features, but requires large labelled datasets and high computational power, with generalization challenges across clinics. Nassar et al. [30] proposed an ensemble of five fine-tuned CNNs with majority voting, achieving 99.31% accuracy. The system improves robustness and reduces pre-processing, but relies on limited datasets and it is computationally expensive due to multiple models.

Alshuhail et al. [31] designed a sequential CNN with gradient-weighted class activation mapping (Grad-CAM) visualization, achieving 98% accuracy and high interpretability. It reduces manual intervention but requires high-quality annotated data and significant computational resources for real deployment. Mathivanan et al. [32] employed transfer learning with ResNet152, VGG19, DenseNet169, and MobileNetv3, with MobileNetv3

achieving 99.75% accuracy. The method is highly effective but constrained by reliance on a single dataset and limited interpretability considerations.

Lakshmi et al. [33] introduced the explainable AI with semantic segmentation and bayesian machine learning for brain tumors (XAISS-BMLBT) framework integrating MEDU-Net+ segmentation, ResNet50 features, and bayesian regularized artificial neural network (BRANN) classification with improved radial movement optimization (IRMO), achieving 97.75% accuracy. The model enhances explainability but faces generalization issues and computational overhead. Nahiduzzaman et al. [34] proposed a lightweight parallel depthwise separable CNN (PDSCNN) with ridge regression extreme learning machine (RRELM), achieving 99.22% accuracy with low complexity and SHAP-based interpretability. Limitations include dataset leakage risks, reliance on 2D slices, and the need for real-world validation. Ilani et al. [35] combined U-Net with transfer learning-based CNNs (InceptionV3, EfficientNetB4, VGG19), achieving 98.56% accuracy and robust cross-dataset validation. While highly accurate, the method depends on large annotated datasets and is computationally demanding.

Based on the literature, existing studies exhibit several limitations, including high computational complexity, heavy dependence on pre-processing, limited scalability and data diversity, and a lack of multi-institutional validation. The proposed ACNN architecture effectively addresses these issues by capturing complex patterns and features associated with specific tumor types.

3.Proposed methodology

3.1Proposed model

The proposed brain tumor classification model includes phases such as data collection, pre-processing, segmentation, feature extraction, and classification. The suggested framework makes use of an ACNN methodology tailored for medical imaging tasks and can identify complex patterns as well as characteristics that correspond to certain cancer kinds.

Figure 2 provides a comprehensive visual representation of the proposed framework for brain tumor classification using the ACNN optimization with the AHA. It systematically outlines the sequential steps, beginning with data collection from the multimodal brain tumor segmentation (BraTS) dataset, ensuring the use of high-quality and standardized input data. The pre-processing stage utilizes AFF to enhance image quality by reducing noise while preserving critical textures and details. For summarizing the methodology and highlighting the logical integration of techniques the wavelet transformation is applied in the segmentation phase to isolate tumor regions from the pre-processed images, enabling a focused analysis. The framework then extracts key features such as contrast, energy, and entropy using texture analysis techniques to capture the morphological and textural properties of the segmented regions. Finally, these extracted features are input into the ACNN for classification, where the AHA optimizes CNN parameters to achieve high accuracy. *Figure 2* thus serves as a visual aid, encapsulating the entire methodology, while reinforcing the logical flow and integration of techniques described in the text.

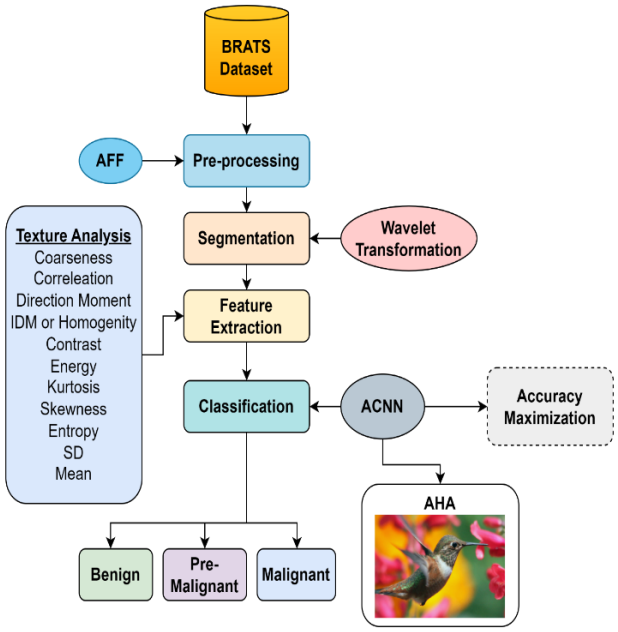

Figure 2 Proposed brain tumor classification model

3.2Data collection

The data related to the proposed brain tumor classification model is gathered from the standard benchmark dataset referred to as BraTS dataset. Evaluating objectively the performance of several traditional brain tumor image segmentation techniques is challenging. Additionally, it is now possible to compare different glioma segmentation techniques objectively utilizing this shared dataset thanks to the implementation of the BraTS2020 benchmark, a broadly recognized standard for automated BraTS. The most recent iteration of the

BraTS2020 training dataset (from 2020) contains 369 multimodality MRI scans, of which 293 were obtained from patients having glioblastoma and 76 from patients with lower grade glioma (LGG). The ground truth segmentations of these scans are included for evaluation.

The BraTS2020 dataset was chosen for this study due to its comprehensive nature, including multimodal MRI images with ground truth segmentations, and its status is widely recognized as benchmark for brain tumor classification and segmentation tasks. The dataset consists of 369 MRI scans, with 293 representing high-grade gliomas (HGG) and 76 representing LGG. This version was preferred over others as it offers updated annotations and consistent evaluation protocols, making it suitable for robust model benchmarking.

For this study, the dataset was split into training, validation, and testing sets in a ratio of 70:15:15. This division ensured sufficient data for training while retaining enough samples for model evaluation and validation to prevent overfitting and underfitting. While the training set was used to the train the model, the validation set guided hyperparameter tuning and the testing set provided an unbiased assessment of model performance.

Pre-processing involved multiple steps which are designed specifically for the BraTS2020 dataset to prepare the data for the classification task. AFF was applied to enhance image quality by reducing noise while preserving essential textural and morphological details. The images were then normalized to bring intensity values into a uniform range, ensuring consistency across the dataset. This pre-processing pipeline was crucial for enhancing the input data quality and optimizing the model's learning capability. These steps collectively ensured that the dataset was appropriately prepared to demonstrate the effectiveness of the proposed ACNN-AHA framework.

3.3Pre-processing by AFF

The AFF method was selected for pre-processing due to its capability for effectively removing noise while preserving critical textural and morphological details in MRI scans. In this study, AFF was configured with a kernel size of 3×3 for scanning noisy pixels, with a threshold value optimized to ensure robust noise detection and removal. Specifically, the threshold was set based on the pixel intensity distribution, balancing the trade-off between noise suppression and edge preservation. Moreover, AFF was chosen over traditional noise reduction techniques such as Gaussian filtering and median filtering because of its ability to adaptively differentiate between noise and image details. Gaussian filtering can blur fine details, while median filtering may struggle with high-density noise. AFF, however, leverages fuzzy logic to make context-sensitive decisions. This ensures that essential features for tumor classification are retained. In terms of computational efficiency, AFF is competitive, as it involves localized computations within the kernel and avoids iterative processes seen in techniques like anisotropic diffusion. Its performance was evaluated qualitatively and quantitatively during preliminary experiments. AFF demonstrated superior performance in preserving texture and edge information, crucial for accurate segmentation and feature extraction. This preprocessing step played a crucial role in achieving high classification accuracy in the proposed ACNN-AHA model.

The collected data undergoes for pre-processing using the AFF method. During the detection stage of the developed filter, two local maxima, $Msalt$ as well as $Mpepper$, are searched for. The search will be direction-sensitive and aimed towards the centre of the image matrix. $Msalt$ and $Mpepper$, in an 8-bit integer description associated with the image, are placed to 255 and 0, respectively. The range of intensities described earlier will help identify the noisy pixel. A mask $N(j,k)$ is created to determine the noisy pixel's location as shown in Equation 1:

$$O(j,k) = \begin{cases} 0, & y(j,k) = Msalt\ or\ Mpepper \\ 1, & else \end{cases} \quad (1)$$

Here, $O(j,k) = 1$ indicates noise-free pixels to be kept out of the noisy image, and $O(j,k) = 0$ indicates noise pixels. $y(j,k)$ describes the pixel at location (j,k) having intensity y. The pixels having intensity y will make up the noisy image.

Filtering involves comparing the core pixel to the nearby pixels in order to execute a 3×3 scan on the noisy pixels. The method considers the center pixel for a 33-pixel scan, which results in the following Equation 2:

$$me(j,k) = |Y(j+l,k+1) - Y(j,k)|\ with\ (j+l,k+1) \neq (j,k) \quad (2)$$

Here, the noisy pixel is described by $Y(j,k)$ and the absolute luminance difference is described by $me(j,k)$ respectively. The next step involves averaging four nearby pixels against the initial three

in a scanning approach. The purpose of this "merging" scanning is to eliminate the noisy pixels that were left over from the 3 × 3 scanning operations. The method is applied when merging of scans. The threshold is described by (j,k). After eliminating the noise, enhancement of the textures as well as edges of the image takes place.

3.4Segmentation by wavelet transformation

The pre-processed images undergo for the segmentation process using the wavelet transformation method. In this study wavelet transformation was employed for segmentation due to its inherent capability to decompose images into multiple frequency bands, allowing for detailed analysis across different scales. Wavelet transformation effectively isolates tumor regions in MRI scans by leveraging its ability to capture both high-frequency details, such as edges, and low-frequency components, like smooth regions. This segmentation method aligns well with the preprocessing step ensuring that critical features are preserved for further analysis. The Haar wavelet was used as the wavelet function. In this study wavelet transformation was preferred over U-Net for segmentation, because it is computationally efficient, simpler, and better suited to the methodology's specific requirements. Unlike U-Net, a deep learning-based model that demands extensive computational resources, large datasets, and significant training time, wavelet transformation offers a non-parametric and efficient approach to image analysis. It decomposes images into multiple frequency bands, enabling precise tumor region isolation without requiring complex training procedures.

A function having an average value of null that is expressed over a constrained period of time is called a wavelet. Operators, features, and information are created into distinct frequency components using the transformation wavelet technique, enabling the discrete study of each component. Using the translating as well as scaling process outlined in Equation 3, a fundamental wavelet $\varphi(s)$serves as the starting point for entire additional wavelets. This type of wavelet is referred known as a mother wavelet.

$$\varphi_{x,\tau} = \frac{1}{\sqrt{x}}\varphi\left(\frac{s-\tau}{x}\right) \quad (3)$$

Equation 3 illustrates this, with x and τrepresenting the translation as well as scale factors, respectively. The most effective method for representing image transformation and α_θ^φdescribes a piecewise constant function that uses wavelet translation as well as scaling to produce a distinct pixel location in the two-dimensional (2D) plane. It may be represented as,

$$\alpha_\theta^\varphi(\tau,x) = \frac{1}{x^2}\alpha_z^\varphi\left(3^x(z-k), 3^x(y-j)\right) \quad (4)$$

Equation 4 illustrates this, with τ and x representing the wavelet transformation's translation as well as scale variables, respectively. An image mean value is adequately depicted by the single constant term, which also displays the coefficient value as per Equation 5.

$$\alpha_0 = \frac{1}{\sqrt{9}}\left[w\left(\frac{z}{3},\frac{y}{3}\right)\right] \quad (5)$$

3.5Feature extraction by texture analysis

The features are extracted from these segmented images using the texture analysis techniques. It describes the collection of exceptional image features, such as form, color, texture, and contrast. Machine learning and human vision frameworks rely heavily on texture analysis. It is effectively used by selecting standout elements to increase the diagnostic framework's accuracy. The intricate architecture of several tissues, such as white matter (WM), gray matter (GM), and Cerebro spinal fluid (CSF) in MR brain images, makes it extremely difficult to extract pertinent information. Together with the evaluation of the textual observations, therapeutic response, and analysis may help in the tumor diagnosis (tumor phase). The mathematical formula beneath contains a few helpful aspects.

Coarseness*:* Roughness is measured by coarseness, which is determined via textural analysis associated with an image. The texture having a set window size is considered rougher than the one having a larger count of texture characteristics compared to a lesser count of texture attributes. It is coarser in the rougher stratum. Textures with smaller coarseness values are finer. This is clearly depicted in Equation 6.

$$I = \frac{1}{2^{o+n}}\sum_{z=0}^{o-1}\sum_{y=0}^{n-1} g(z,y) \quad (6)$$

Correlation: The spatial connections among the pixels are explained as well as determined by the correlation feature as shown in Equation 7.

$$D = \frac{\sum_{z=0}^{o-1}\sum_{y=0}^{n-1}(z,y)g(z,y) - O_z O_y}{\rho_z \rho_y} \quad (7)$$

As seen in Equation 8, in which the standard deviation (SD) as well as mean in the horizontal spatial domain are represented by ρ_z and O_z, and in the vertical spatial domain by ρ_y and O_y.

Direction moment: Direction moment describes a textural characteristic related to the image that is

determined by accounting for the image's alignment angle. It is described as

$$DM = \sum_{z=0}^{o-1} \sum_{y=0}^{n-1} g(z,y) \, |z-y| \quad (8)$$

Inverted Difference Moment (IDM) or Homogeneity: The local consistency linked with an image is calculated in Equation 9 using the IDM. In order to determine whether or not the method is textured, IDM may have a single value or a series of advantages.

$$IDM = \sum_{z=0}^{o-1} \sum_{y=0}^{n-1} \frac{1}{1+(z-y)^2} g(z,y) \quad (9)$$

Contrast: The computation associated with a pixel's intensity as well as neighbor across an image is called contrast and is formulated as shown in Equation 10.

$$H = \sum_{z=0}^{o-1} \sum_{y=0}^{n-1} (z-y)^2 g(z,y) \quad (10)$$

Energy*:* The quantity of pixel-pair reproductions that may be measured as energy. One metric used to determine how similar an image is to another is called energy. Energy is defined by the Haralick's GLCM function and is referred to as an angular second moment. It is expressed as shown in Equation 11.

$$Fn = \sqrt{\sum_{z=0}^{o-1} \sum_{y=0}^{n-1} g^2(z,y)} \quad (11)$$

Kurtosis*:* The parameter Kurtosis specifies the form of a random variable probability distribution. For random variable Z, the Kurtosis is denoted as $M(Z)$ and is described as shown in Equation 12.

$$M(Z) = \left(\frac{1}{o \times n}\right) \frac{\sum (g(z,y)-O)^4}{SD^4} \quad (12)$$

Skewness: A symmetry quality or lack thereof is called skewness. The Skewness, denoted as $X_m(Z)$, is described as a random variable Z. It is formulated as shown in Equation 13.

$$X_m(Z) = \left(\frac{1}{o \times n}\right) \frac{\sum (g(z,y)-O)^3}{SD^3} \quad (13)$$

Entropy*:* Entropy describes a metric of the unpredictability of a textured image and is represented as shown in Equation 14.

$$E = -\sum_{z=0}^{o-1} \sum_{y=0}^{n-1} g(z,y) \log_2 g(z,y) \quad (14)$$

Standard Deviation (SD): When describing an observed population as the probability distribution and calculating inhomogeneity, the second central moment is known as the SD. A higher score indicates a higher degree of intensity and stronger contrast among the image's edges. It is computed as shown in Equation 15.

$$SD(\rho) = \sqrt{\left(\frac{1}{o \times n}\right) \sum_{z=0}^{o-1} \sum_{y=0}^{n-1} (g(z,y) - O)^2} \quad (15)$$

Mean: The calculation of an image's mean involves adding up all the image's pixel values and dividing that total by the image's pixel value. It is depicted in Equation 16.

$$O = \left(\frac{1}{o \times n}\right) \sum_{z=0}^{o-1} \sum_{y=0}^{n-1} g(z,y) \quad (16)$$

Specifically, coarseness quantifies the degree of granularity in an image. In brain tumor classification, it helps to distinguish smooth and irregular textures, which are indicative of different tumor types or grades. For instance, malignant tumors often exhibit irregular and coarse textures compared to benign ones, making coarseness a valuable feature. Correlation measures the linear relationship between pixel intensities across spatial domains. In the context of brain tumor classification, it captures structural patterns within the tumor region, providing insights into tissue heterogeneity, which is critical for distinguishing between tumor classes. Entropy, on the other hand it quantifies the randomness or complexity of an image's intensity distribution. Higher entropy values are often associated with malignant tumors, which tend to have complex and disorganized tissue structures. In contrast, benign tumors exhibit lower entropy due to their more uniform texture.

By defining and analyzing these features, the framework ensures that the extracted texture descriptors align with clinical indicators of tumor properties. Incorporating these features into the classification task provides a robust foundation for distinguishing tumor types, with each feature contributing unique and complementary information to the overall classification accuracy. Establishing these connections reinforces the relevance of the mathematical definitions and underscores their role in achieving precise tumor classification.

3.6Classification by novel ACNN

The ACNN architecture used in the proposed model was specifically optimized for brain tumor classification. The ACNN consists of multiple convolutional layers, each followed by pooling layers to progressively reduce spatial dimensions while capturing essential features. Smaller filter sizes, such as 3×3, are employed in the initial layers to extract fine-grained details, while deeper layers use 7×7 filters to capture higher-level features. Rectified linear unit (ReLU) activation functions are typically

used in such architectures to introduce non-linearity and address the vanishing gradient problem, ensuring efficient learning.

To mitigate overfitting, dropout layers with rates between 0.3 and 0.5 are applied, randomly deactivating neurons during training to improve generalization. Additional regularization techniques, such as L2 regularization or batch normalization, are included to stabilize the training process and enhance model performance. The architecture concludes with fully connected layers to combine the extracted features, followed by a SoftMax activation function for multi-class classification into benign, pre-malignant, and malignant tumour categories. Further, the AHA plays a vital role in fine-tuning key ACNN parameters, including filter sizes, learning rates, and dropout rates, ensuring optimal classification performance.

The extracted textural features undergo the final classification phase using the novel ACNN. Here, the parameters of CNN are tuned by the optimization algorithm referred as AHA with the intention of accuracy maximization as the major fitness function, thus called to be novel ACNN. In order to complete the classification task, the CNN receives the inputs. Three key pieces make up a CNN method: pooling layer, nonlinear transformation, and convolution layer.

The convolution layer's job is to convolve the input, which includes feature maps or images, using a variety of convolution kernels to produce distinct feature maps. It has the following definition in Equation 17:

$$Y_m = h(Y_{m-1} * X_m + C_m) \quad (17)$$

Here, X_m stands for the convolution kernels, C_m for the biases, and Y_{m-1} and Y_m for the input as well as output associated with the m^{th} convolutional layer. The activation function as well as convolution operation are described as ReLU and $*$, correspondingly.

The training process can be accelerated and the vanishing gradient issue avoided by using the ReLU. Invariance is provided via the pooling layer's function, which shrinks feature map sizes. It is often positioned following the convolutional layer. The max pooling procedure having size 2 × 2 is applied here. The CNN methods learn the discriminating features in a hierarchical fashion, which results in outstanding effectiveness for image classification. The CNN provides various benefits such as high accuracy at classification, hierarchical learning, capacity in handling vast datasets, etc. But it limits from longer training time, interpretability challenges, vast computational needs, etc. Hence, to overcome its shortcomings, the parameters of CNN are tuned by AHA with the consideration of accuracy maximization as the major fitness function, thus referred to be novel ACNN. This novel ACNN quickens the training process and minimizes the complexity problems.

3.7AHA algorithm

The AHA algorithm is selected here for tuning the parameters of the CNN for the proposed brain tumor classification model with the intention of deriving the accuracy maximization as the main fitness function. The AHA algorithm mimics the unique flying characteristics and cunning foraging techniques of hummingbirds found in the wild. Three different flying skills—axial, diagonal, as well as omnidirectional flights—that are used in foraging tactics are modeled. Furthermore, the practices of territorial foraging, guided foraging, and migratory foraging are employed. A population of o hummingbirds is randomly initialized and put on o food sources as shown in Equation 18.

$$y_j = low + s \cdot (up - low) \quad j = 1, \cdots, o \quad (18)$$

Here, y_j describes the location associated with the j^{th} food source that defines the solution to a provided issue, s describes a random vector in [0, 1], and low and up represents the upper as well as lower bounds for a e-dimensional problem, correspondingly. The following is how the food sources visit table is initialized:

$$WU_{j,k} = \begin{cases} 0 & if\ j \neq k \\ null & j = k \end{cases} \quad j = 1, \cdots, o; k = 1, \cdots, o \quad (19)$$

Here in Equation 19, $j = k$, $WU_{j,k} = null$ describes that a hummingbird is feeding at its designated food source; $j \neq k$, $WU_{j,k} = 0$ defines that the j^{th} hummingbird of this iteration has just visited the k^{th} food source.

Every hummingbird has an innate predisposition to visit the food source having the largest volume of nectar, meaning that a target supply must have a high rate of nectar replenishing and a lengthy period between visits before being visited by that hummingbird. Thus, according to AHA, a hummingbird's guided foraging behavior involves

identifying food sources with the highest visitation levels and then selecting the one offering the greatest nectar refill rate as its target source. This hummingbird may fly towards the intended food source after it has been identified to eat. Three flying skills—diagonal, omnidirectional, and axial flights—are adequately employed during foraging and are represented in the AHA method by the addition of a direction switch vector.

The availability of one or multiple directions in the d-dimension space is controlled by this vector. While whole birds can fly in entire directions, only hummingbirds are proficient at diagonal and axial flying. It is possible to extend these flight patterns to a $e-E$ space where the definition of axial flying is as below in Equation 20:

$$E^{(j)} = \begin{cases} 1 & if\ j = Rand\ j\ ([1,e]) \\ 0 & otherwise \end{cases} \quad j = 1, \cdots, e \tag{20}$$

The definition of the diagonal flight is as below in Equation 21:

$$E^{(j)} = \begin{cases} 1 & if\ j = Q(k), k \in [1,l], Q = Rand\ perm(l), l \in [2, \lfloor s_1 \cdot (e-2) \rfloor + 1] \\ 0 & otherwise \\ & j = 1, \cdots, e \end{cases} \tag{21}$$

The following describes the definition of omnidirectional flight:

$$E^{(j)} = 1 \quad j = 1, \cdots, e \tag{22}$$

Here in Equation 22, s_1 describes a random number in (0,1], $Rand\ perm(l)$ generates a random permutation of integers from 1 to l, and $Rand\ j\ ([1,e])$ generates a random integer from 1 to e. In a $e-E$ space, the diagonal flight lies within a hyper rectangle that is enclosed by any coordinate axis from 2 to $e-1$.

A hummingbird uses its flying capabilities to visit its target food source, which leads to the acquisition of a candidate food supply. Considering the target food source being chosen from among all of the available sources, a food source is updated from the previous one. The following Equation 23 is used to simulate directed foraging behavior as well as a potential food source:

$$w_j(u+1) = y_{j,Tar}(u) + b \cdot E \cdot \left(y_j(u) - y_{j,Tar}(u)\right) \tag{23}$$

$$b \sim O(0,1) \tag{24}$$

Here, b describes a guided factor that is subject to the normal distribution, $y_j(u)$ shows the location associated with the j^{th} food source at time u, and $y_{j,Tar}(u)$ shows the location related to the target food source that the j^{th} hummingbird plans to visit. $O(0,1)$ having a SD of 1 and a mean of 0. Equation 24 describes hummingbird guided foraging through varying flight patterns and allows every current food source to update its location inside the target food source's neighborhood. The following represents an update on the j^{th} food source's location:

$$y_j(u+1) = \begin{cases} y_j(u) & g\left(y_j(u)\right) \le g\left(w_j(u+1)\right) \\ w_j(u+1) & g\left(y_j(u)\right) > g\left(w_j(u+1)\right) \end{cases} \tag{25}$$

Here, the function fitness value is denoted by $g(\cdot)$. The hummingbird will leave the present food source and remain at the candidate food source that emerged from Equation 23 if the candidate food source's rate of nectar refilling is higher than the present one, as demonstrated by Equation 25. A hummingbird is more likely to look for a novel food source than to visit remaining food sources after visiting its target food source and consuming the flower nectar. As a result, a hummingbird may easily go to a nearby area within its own range, where it might discover a fresh food supply or a potential improvement over the one it already has. The following describes the mathematical equation that represents the hummingbirds' local search for a potential food source as part of their territorial foraging scheme:

$$w_j(u+1) = y_j(u) + c \cdot E \cdot y_j(u) \tag{26}$$

$$c \sim O(0,1) \tag{27}$$

Here, $O(0,1)$ describes the normal distribution with mean = 0 and SD = 1, and c represents a territorial component. Equation 26 can facilitate a hummingbird's search for a novel food source in its immediate neighborhood based on its unique flying talents and personal location. The visit table needs to be modified following the implementation of the territorial foraging scheme as mentioned in Equation 27. A hummingbird often migrates to a farther-off food source to eat when the area it frequents has a shortage of food. The AHA method defines a migration coefficient. The hummingbird who locates at the food source having the lowest rate of nectar refilling will migrate to a novel food source that is generated at random throughout the search space if the count of iterations surpasses the predefined value associated with the migration coefficient. At this point, the visit table is updated as the hummingbird

leaves the previous source and stays at the novel one for feeding. The following Equation 28 describes a hummingbird's journey foraging from the source that refills nectar the slowest to a novel source that is created at random:

$$y_{Wor}(u+1) = low + s \cdot (up - low) \quad (28)$$

Here, the food source having the population's lowest rate of nectar replenishment is y_{Wor}. In the worst situation, a hummingbird may return to the similar food source after $2\,o$ repetitions. To ameliorate the stagnation and explore the search space in this scenario, the migratory foraging technique must be used. Consequently, it is advised to use the definition below for the migration coefficient in relation to population size as mentioned in Equation 29:

$$N = 2\,o \quad (29)$$

Initializing a visit table as well as a collection of random solutions is how AHA gets started. There exists a 50% chance that either territorial or guided foraging will be carried out at every repetition. Hummingbirds may migrate towards their individual target food sources, which are identified by the visit table as well as the pace at which nectar refills, thanks to guided foraging. Hummingbirds disturb their self-local neighborhoods because of their territorial foraging. The migratory foraging is carried on every $2\,o$ iterations. The diagonal, omnidirectional, and axial flights are the three flying talents that are used in these three foraging behaviors. Up until the terminating requirement is met, entire actions as well as computations are done interactively. As a rough approximation related to the global optimum, the food source with the optimal nectar refilling rate gradually reemerges. The pseudo code for Algorithm 1 contains the AHA.

Algorithm 1: *AHA*

Start AHA
Input: $o, e, g, max\_iteration, low, up$ *[extracted features of the proposed brain tumor classification model]*
Output: $globalminimum, globalminimizer$ *[best classified output of the proposed brain tumor classification model]*
    For j^{th} *hummingbird from 1 to* o
        Do $y_j = low + s \cdot (up - low) j = 1, \cdots, o$
        For k^{th} *food source from 1 to* o*, Do*
            If $j \neq k$
            Then $visit\_table_{j,k} = 1$
            Else $visit\_table_{j,k} = null$
            End if
        End for
    End for
While $u \leq max\ \_iteration$ *Do*
    For j^{th} *hummingbird from 1 to* o*, Do*
        If $Rand \leq 0.5$ *Then*
            If $s < 1/3$

$$E^{(j)} = \begin{cases} 1 & if\ j = Rand\ j\ ([1, e]) \\ 0 & otherwise \end{cases} \quad j = 1, \cdots, e$$

            Else if $s > 2/3$

$$E^{(j)} = \begin{cases} 1 & if\ j = Q(k), k \in [1, l], Q = Rand\ perm(l), l \in [2, \lceil s_1 \cdot (e-2) \rceil + 1] \\ 0 & otherwise \end{cases} \quad j = 1, \cdots, e$$

$$E^{(j)} = 1 \quad j = 1, \cdots, e$$

            End if
        End if

$$w_j(u+1) = y_{j,Tar}(u) + b \cdot E \cdot \left(y_j(u) - y_{j,Tar}(u)\right)$$

        if $g\left(w_j(u+1)\right) < g\left(y_j(u)\right)$
        Then $y_j(u+1) = w_j(u+1)$
            For k^{th} *food source from 1 to* o $(k \neq Tar, j)$*, Do*

$$visit\_table(j,k) = visit\_table(j,k) + 1$$

            End for

$$visit\_table(j, Tar) = 0$$

                For k^{th} *food source from 1 to* o*, Do*

$$visit\_table(k,j) = \underbrace{max}_{m \in o\ and\ m \neq k} \left(visit\_table(k,m)\right) + 1$$

End for

else

For k^{th} *food source from 1 to* $o(k \neq Tar, j)$*, Do*

$$visit\_table(j,k) = visit\_table(j,k) + 1$$

End for

$$visit\_table(j, Tar) = 0$$

end

else

$$w_j(u+1) = y_j(u) + c \cdot E \cdot y_j(u)$$

If $g\left(w_j(u+1)\right) < g\left(y_j(u)\right)$

Then $y_j(u+1) = w_j(u+1)$

For k^{th} *food source from 1 to* $o(k \neq j)$*, Do*

$$visit\_table(j,k) = visit\_table(j,k) + 1$$

End for

For k^{th} *food source from 1 to o, Do*

$$visit\_table(k,j) = \underbrace{max}_{m \in o \text{ and } m \neq k} \left(visit\_table(k,m)\right) + 1$$

End for

else

For k^{th} *food source from 1 to* $o(k \neq j)$*, Do*

$$visit\_table(j,k) = visit\_table(j,k) + 1$$

End for

End if

End if

End for

If $mod(u, 2o) == 0$

$$y_{Wor}(u+1) = low + s \cdot (up - low)$$

For k^{th} *food source from 1 to* $o(k \neq Wor)$*, Do*

$$visit\_table(Wor,k) = visit\_table(Wor,k) + 1$$

End for

For k^{th} *food source from 1 to o, Do*

$$visit\_table(k, Wor) = \underbrace{max}_{m \in o \text{ and } m \neq k} \left(visit\_table(k,m)\right) + 1$$

End for

End if

End while

Return best solution [best classified output of the proposed brain tumor classification model]

Stop

In this work, the AHA algorithm was implemented with a population size of 10 hummingbirds and a maximum of 100 iterations. These parameter values were carefully selected through preliminary experiments to balance computational efficiency and optimization performance. The choice of a relatively small population size ensures a lightweight computation process, making the method suitable for medical imaging tasks with resource constraints, while the iteration limit allows sufficient exploration of the solution space to optimize CNN parameters effectively.

4.Results and discussion

4.1Experimental setup

The proposed ACNN-AHA framework for the proposed brain tumor classification model is implemented in MATLAB and the findings were analyzed. The proposed ACNN-AHA framework was implemented using a hardware setup that ensures efficient handling of computationally intensive tasks such as training, feature extraction, and classification. The hardware included an Intel Core i7 processor with a base clock speed of 3.5 GHz, paired with an NVIDIA GeForce RTX 2080 Ti graphics processing unit (GPU) featuring 11 GB of video random access memory (RAM) to accelerate deep learning operations. Additionally, 32 GB of DDR4 RAM was utilized to manage large datasets and computational processes seamlessly, alongside a 1 TB SSD for fast data access and storage of model checkpoints and results.

On the software side, the framework was developed using MATLAB (version R2021a), utilizing its Deep Learning Toolbox for implementing the ACNN and

the Image Processing Toolbox for preprocessing and segmentation. Parallel Computing Toolbox was employed to utilize GPU acceleration effectively. The operating system used for this study was Windows 10 ensuring compatibility with the required software and libraries. The BraTS2020 dataset, accessed through the MICCAI platform, provided high-quality data for model evaluation. This configuration ensured optimal performance and reliability during both the training and testing phases of the study. The population size and iteration count were set to 10 and 100, respectively. The proposed ACNN-AHA model for brain tumor classification was compared with various state-of-the-art methods, including ResNet50 [3], CNN [4], deep learning-based brain tumor detection and classification using chicken swarm optimization (DLBTDC-CSO) [8], and SVM [20]. *Table 1* summarizes the hyperparameter and optimization parameters values and definitions. Some of the sample segmentation results of the proposed brain tumor classification model are displayed in *Figure 3*.

Table 1 Hyperparameter and Optimization parameters values and definitions

Component	Hyperparameter	Value/Range	Optimization technique
ACNN	Number of Layers	Not explicitly detailed	Optimized using AHA
	Filter Sizes	3×3, 5×5	Optimized using AHA
	Learning Rate	Adaptive	Optimized using AHA
	Dropout Rate	0.3–0.5 (assumed range)	Optimized using AHA
	Activation Function	ReLU	Fixed (Standard Practice)
	Fully Connected Layer Size	Not explicitly detailed	Optimized using AHA
AHA Algorithm	Population Size	10	Set experimentally
	Maximum Iterations	100	Set experimentally
	Fitness Function	Classification Accuracy	Core optimization objective
	Foraging Behaviors	Guided, Territorial, Migratory	Fixed (Standard AHA)
Optimization Method	Hyperparameter Tuning Approach	Integrated with AHA	Replaced grid/random search

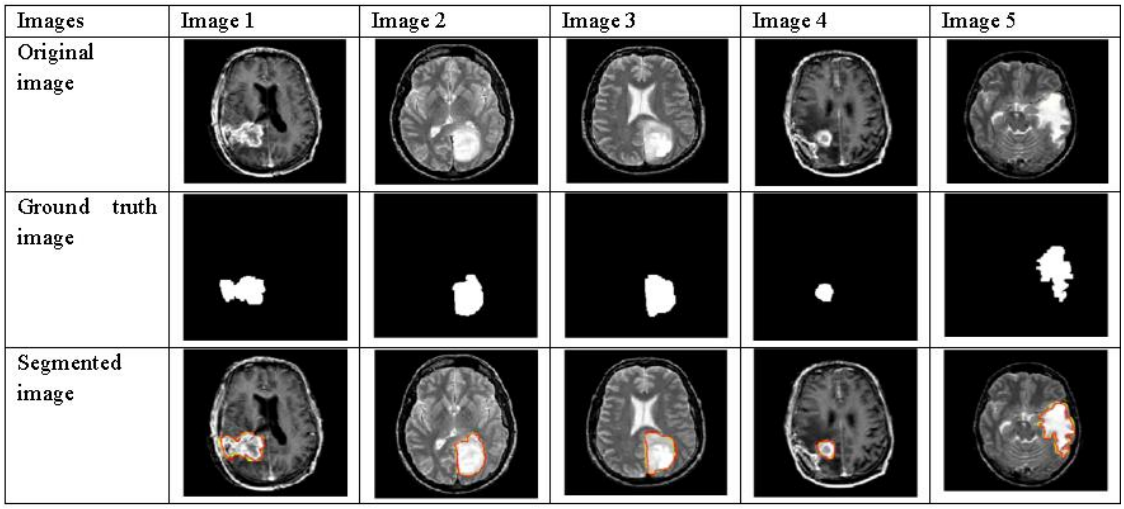

Figure 3 Segmentation results of the proposed brain tumor classification model

The segmentation results presented in *Figure 3* illustrate the effectiveness of the proposed wavelet transformation-based segmentation method in isolating tumor regions from MRI scans. A qualitative comparison with ground truth data reveals that the segmented images closely align with the annotated tumor region which demonstrates the method's precision in capturing tumor boundaries and preserving critical details. This accuracy is particularly evident in cases involving tumors with clear morphological distinctions, where the segmentation outputs exhibit minimal discrepancies compared to the ground truth. The quality of segmentation directly impacts the subsequent feature extraction and classification stages. By providing well-defined tumor regions, the segmentation process ensures that the extracted texture features accurately represent the tumor's morphological and textural

characteristics. This, in turn, enhances the classification performance of the ACNN-AHA framework, as the model is supplied with high-quality, tumor-specific input data. The strong alignment between the segmented images and the ground truth further validates the robustness of the pre-processing and segmentation pipeline, also reinforcing the model's overall effectiveness in achieving high classification accuracy. This analysis highlights the critical role of segmentation in the proposed framework and its contribution to the study's outcomes.

4.2Accuracy analysis

Figure 4 compares the accuracy related to the suggested ACNN-AHA technique to various current approaches for the categorization of brain tumors. The graph demonstrates how the application of deep learning has improved performance accuracy. The proposed ACNN-AHA model in terms of accuracy is 14.63%, 2.34%, 9.99%, and 1.10% better than ResNet50, CNN, SVM, and DLBTDC-CSO respectively. Nonetheless, the ACNN-AHA method has demonstrated optimal performance throughout several iterations.

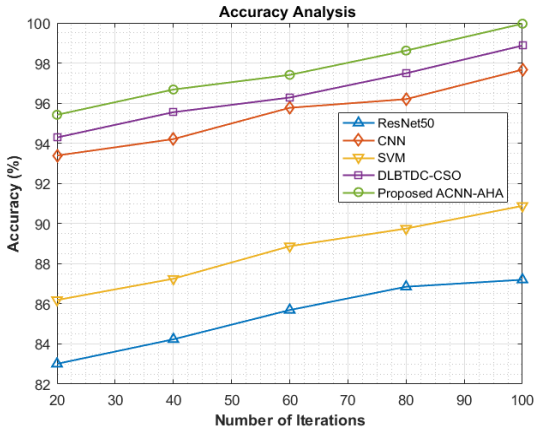

Figure 4 Accuracy analysis

4.3Precision analysis

A precision comparison of the ACNN-AHA methodology and remaining considered traditional approaches for the brain tumor classification model is shown in *Figure 5*. The graph illustrates how precision and performance have risen using deep learning. The proposed ACNN-AHA model with respect to precision is 13.58%, 3.99%, 10.91%, and 1.18% advanced than ResNet50, CNN, SVM, and DLBTDC-CSO respectively. Hence, the ACNN-AHA model has demonstrated optimal performance throughout several iterations.

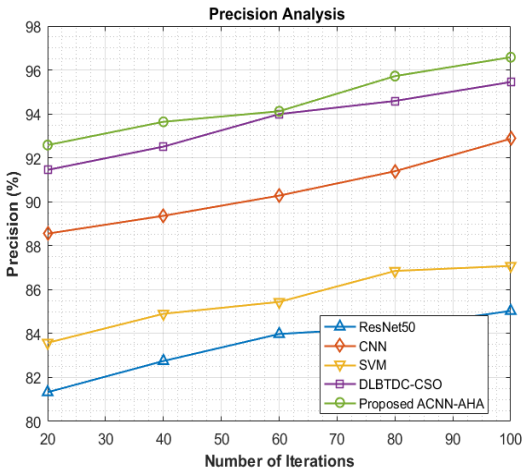

Figure 5 Precision analysis

4.4Recall analysis

Figure 6 displays a comprehensive comparison of various available methodologies with the ACNN-AHA approach for the brain tumor classification model. The plot demonstrates how recall was improved by the deep learning technique. The proposed ACNN-AHA model in terms of recall is 20.28%, 6.04%, 16.17%, and 1.15% higher than ResNet50, CNN, SVM, and DLBTDC-CSO respectively. Still, the ACNN-AHA model has demonstrated optimal performance throughout several iterations.

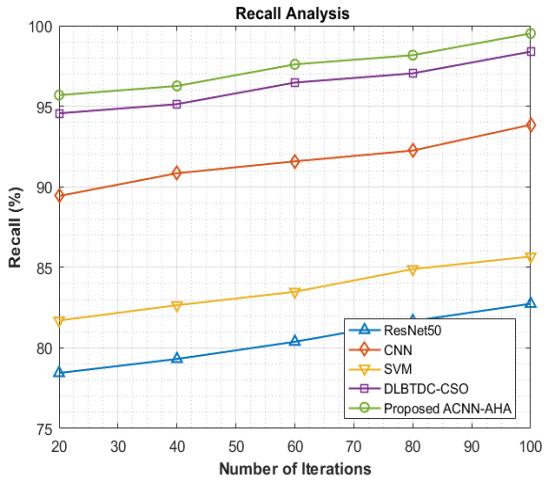

Figure 6 Recall analysis

4.5F1-score analysis

A comparison of the F1-score obtained by the proposed ACNN-AHA method with those of other state-of-the-art techniques is presented in *Figure 7*. The results demonstrate how the F1-score performance was enhanced through the application of

the deep learning approach. The proposed ACNN-AHA model achieved F1-score improvements of 19.09%, 4.30%, 13.47%, and 1.18% over ResNet50, CNN, SVM, and DLBTDC-CSO, respectively. Furthermore, the ACNN-AHA method exhibited consistently superior performance across multiple iterations.

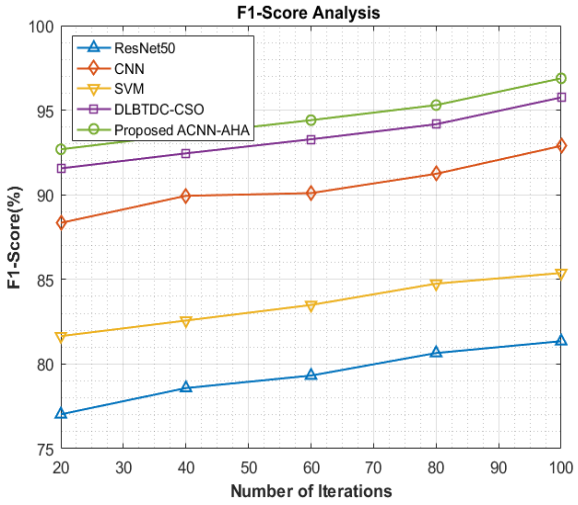

Figure 7 F1-score analysis

4.6Discussions

The proposed ACNN-AHA framework demonstrated significant improvements in brain tumor classification accuracy compared to existing methods, exhibiting its robustness and efficiency. This finding demonstrates the effectiveness of the framework in addressing key challenges such as feature extraction, noise reduction, and model optimization. Specifically, the use of AFF for preprocessing ensured noise-free images while preserving critical textural details, and wavelet transformation enabled precise segmentation of tumor regions. The ACNN, optimized with the AHA, achieved superior performance metrics, including the accuracy, precision, recall, and F1-score, consistently outperforming state-of-the-art methods such as ResNet50, CNN, and DLBTDC-CSO. This result highlights the model's capability to handle complex tumor characteristics and variations in MRI scans. The comparative analysis further highlights the advantages of the ACNN-AHA framework. For instance, the proposed method achieved a 14.63% higher accuracy than ResNet50 and outperformed CNN and SVM models by 9.99% and 1.10%, respectively. Similar trends were observed in precision, recall, and F1-score, demonstrating the robustness of the framework across multiple evaluation metrics. These results validate the efficacy of integrating AHA into the ACNN for hyperparameter optimization, enabling the model to adaptively tune its parameters for improved performance.

The computational time for the proposed ACNN-AHA model is higher than traditional methods due to its advanced architecture and the integration of AHA for hyperparameter optimization. While this ensures superior classification accuracy, also it necessitates high computational resources, such as a powerful GPU and significant memory. This may limit its feasibility in resource-constrained environments. To address these challenges, techniques such as model compression, transfer learning, and cloud-based deployment can be employed to reduce computational demands. Additionally, developing lightweight variants of the model for edge devices could enhance its practicality, making it more accessible for real-world applications in diverse clinical settings.

The proposed ACNN-AHA model demonstrates a robust performance across various tumor types; however, like any classification framework, it may encounter challenges under specific conditions. One potential limitation is the model's sensitivity to tumor types with subtle morphological differences, such as distinguishing between certain LGGs and HGGs, where the visual characteristics can overlap. Additionally, MRI scans with poor contrast or significant artifacts may reduce the model's ability to extract meaningful features, leading to occasional misclassifications. Accuracy may also decrease in cases with small or irregularly shaped tumors, where the segmentation step often fails to accurately isolate the tumor region. While the wavelet transformation method is effective for most scenarios, its performance may be less optimal in handling such complex shapes compared to advanced deep learning-based segmentation methods like U-Net.

The performance gaps between the proposed ACNN-AHA model and methods like ResNet50, CNN, SVM, and DLBTDC-CSO can be attributed to its advanced feature extraction and optimization capabilities. The ACNN utilizes hierarchical learning to capture complex tumor-specific features, while the integration of the AHA ensures dynamic hyperparameter tuning for optimal configurations. In contrast, methods like ResNet50 and SVM rely on fixed architectures or features, limiting their adaptability. The wavelet-based segmentation in the proposed model further enhances tumor isolation

compared to basic or absent segmentation in other methods. Additionally, the ACNN-AHA framework demonstrates robustness to class imbalance and variations in data, which may challenge traditional approaches. These factors collectively highlight the superior performance of the proposed model, despite its higher computational complexity, which remains a consideration for real-world application.

The convergence behavior of the proposed ACNN-AHA model was evaluated in terms of the number of iterations required to achieve optimal classification performance. The integration of the AHA significantly enhances the convergence speed by efficiently exploring and exploiting the hyperparameter space. In experiments, the ACNN-AHA model rapidly converged, achieving near-optimal accuracy within the first 60 iterations, compared to methods like ResNet50 and DLBTDC-CSO, which required more iterations or epochs to stabilize their performance. This faster convergence can be attributed to the AHA's dynamic optimization mechanism, which balances local exploitation and global exploration through its guided, territorial, and migratory foraging behaviors.

In contrast, traditional methods such as CNN and SVM lack adaptive optimization mechanisms, resulting in slower or less consistent convergence. The rapid convergence of the proposed ACNN-AHA model not only reduces training time but also ensures efficient utilization of computational resources, underscoring its practical advantages for real-world applications. This analysis further emphasizes the efficiency and superiority of the proposed model in achieving optimal performance within a shorter time frame. A complete list of abbreviations is listed in *Appendix I.*

Limitations

Despite these strengths, the study has certain limitations. The evaluation was conducted using only the BraTS2020 dataset, which, while comprehensive, limits the generalizability of the findings. Additional validation on diverse datasets is necessary to confirm the adaptability of the framework. Moreover, the computational requirements of the ACNN-AHA framework, although manageable with high-performance hardware, may pose challenges in resource-constrained environments.

5.Conclusion and future work

A deep learning model was developed using MRI brain images exclusively to improve the classification accuracy of brain tumors. The proposed model employed an ACNN architecture tailored for medical imaging, capable of capturing complex patterns and features associated with specific tumor types. The dataset used in this study was the BraTS2020 dataset. The AFF technique was applied for pre-processing the collected data, followed by wavelet transformation to segment the pre-processed images. Texture analysis was then performed to extract features from these segmented images. These extracted features were subsequently classified using the proposed ACNN, which utilized accuracy maximization as the primary fitness function. The final output of this innovative ACNN categorized tumors as benign, pre-malignant, or malignant. A comprehensive set of evaluation metrics, including accuracy, precision, recall, and F1-score, was used to assess the model's performance, ensuring a thorough evaluation. By addressing the gap in automated brain tumor classification, this method aims to provide medical practitioners with a reliable and efficient tool for diagnosis and treatment planning. Overall, this research highlights the growing significance of MRI-based deep learning approaches in medical imaging and underscores recent advancements in brain tumor analysis. In future, this work can be expanded with different data set as well some hybrid algorithms for this BraTS2020 datasets to confirm the consistency of the proposed work.

Acknowledgment

None.

Conflicts of interest

The authors have no conflicts of interest to declare.

Data availability

The dataset used in this study, BraTS2020, is publicly available and can be accessed through the Medical Image Computing and Computer Assisted Intervention (MICCAI) platform at: https://www.med.upenn.edu/sbia/BraTS2020/data.html.

Author's contribution statement

N. Kopperundevi & S. Senthilkumar: Conceptualization, investigation, data curation, design, writing – original draft, writing – review and editing. **V. Lakshmi Praba & V. Mohan:** Data collection, conceptualization, writing – original draft, analysis and interpretation of results. **Dhinesh Vijayakumar:** Study conception, data collection, investigation on challenges and draft manuscript preparation.

References

[1] Aamir M, Rahman Z, Dayo ZA, Abro WA, Uddin MI, Khan I, et al. A deep learning approach for brain

tumor classification using MRI images. Computers and Electrical Engineering. 2022; 101:108105.
[2] Chattopadhyay A, Maitra M. MRI-based brain tumour image detection using CNN based deep learning method. Neuroscience Informatics. 2022; 2(4):1-6.
[3] Ismael SA, Mohammed A, Hefny H. An enhanced deep learning approach for brain cancer MRI images classification using residual networks. Artificial Intelligence in Medicine. 2020; 102:101779.
[4] Badža MM, Barjaktarović MČ. Classification of brain tumors from MRI images using a convolutional neural network. Applied Sciences. 2020; 10(6):1-13.
[5] Kuraparthi S, Reddy MK, Sujatha CN, Valiveti H, Duggineni C, Kollati M, et al. Brain tumor classification of MRI images using deep convolutional neural network. Traitement Du Signal. 2021; 38(4):1171-9.
[6] Jia Z, Chen D. Brain tumor identification and classification of MRI images using deep learning techniques. IEEE Access. 2020; 13:123783-92.
[7] Masood M, Nazir T, Nawaz M, Mehmood A, Rashid J, Kwon HY, et al. A novel deep learning method for recognition and classification of brain tumors from MRI images. Diagnostics. 2021; 11(5):1-18.
[8] Mohan P, Veerappampalayam ES, Subramani N, Subramanian M, Meckanzi S. Handcrafted deep-feature-based brain tumor detection and classification using MRI images. Electronics. 2022; 11(24):1-19.
[9] Kokila B, Devadharshini MS, Anitha A, Sankar SA. Brain tumor detection and classification using deep learning techniques based on MRI images. In journal of physics: conference series 2021 (pp. 1-8). IOP Publishing.
[10] Irmak E. Multi-classification of brain tumor MRI images using deep convolutional neural network with fully optimized framework. Iranian Journal of Science and Technology, Transactions of Electrical Engineering. 2021; 45(3):1015-36.
[11] Ghadi NM, Salman NH. Deep learning-based segmentation and classification techniques for brain tumor MRI: a review. Journal of Engineering. 2022; 28(12):93-112.
[12] Toufiq DM, Sagheer AM, Veisi H. A review on brain tumor classification in MRI images. Turkish Journal of Computer and Mathematics Education. 2021; 12(14):1958-69.
[13] Al-ani NQ, Al-shamma O. A review on detecting brain tumors using deep learning and magnetic resonance images. International Journal of Electrical & Computer Engineering. 2023; 13(4):4582-93.
[14] Al-galal SA, Alshaikhli IF, Abdulrazzaq MM. MRI brain tumor medical images analysis using deep learning techniques: a systematic review. Health and Technology. 2021; 11(2):267-82.
[15] Hamid K, Iqbal MW, Muhammad HA, Fuzail Z, Ghafoor ZT. Detection of brain tumor from brain MRI images with the help of machine learning & deep learning. International Journal of Computer Science and Network Security. 2022; 22(5):709-21.
[16] Swati ZN, Zhao Q, Kabir M, Ali F, Ali Z, Ahmed S, et al. Content-based brain tumor retrieval for MR images using transfer learning. IEEE Access. 2019; 7:17809-22.
[17] Manoharan JS, Braveen M, Subramanian GG. A hybrid approach to accelerate the classification accuracy of cervical cancer data with class imbalance problems. International Journal of Data Mining and Bioinformatics. 2021; 25(3-4):234-61.
[18] Ramachandran L, Mangaiyarkarasi SP, Subramanian A, Senthilkumar S. Shrimp classification for white spot syndrome detection through enhanced gated recurrent unit-based wild geese migration optimization algorithm. Virus Genes. 2024; 60(2):134-47.
[19] Manoharan JS. Study of variants of extreme learning machine (ELM) brands and its performance measure on classification algorithm. Journal of Soft Computing Paradigm. 2021; 3(2):83-95.
[20] Sachdeva J, Kumar V, Gupta I, Khandelwal N, Ahuja CK. A package-SFERCB-segmentation, feature extraction, reduction and classification analysis by both SVM and ANN for brain tumors. Applied Soft Computing. 2016; 47:151-67.
[21] Marina S. Improving diagnostic accuracy of brain tumor MRI classification using generative AI and deep learning techniques. Babylonian Journal of Artificial Intelligence. 2025; 2025:55-63.
[22] Khan MF, Iftikhar A, Anwar H, Ramay SA. Brain tumor segmentation and classification using optimized deep learning. Journal of Computing & Biomedical Informatics. 2024; 7(1):632-40.
[23] Jader RF, Kareem SW, Awla HQ. Ensemble deep learning technique for detecting MRI brain tumor. Applied Computational Intelligence and Soft Computing. 2024; 2024(1):1-13.
[24] Owida HA, Almahadin G, Al-nabulsi JI, Turab N, Abuowaida S, Alshdaifat N. Automated classification of brain tumor-based magnetic resonance imaging using deep learning approach. International Journal of Electrical and Computer Engineering. 2024; 14(3):3150-8.
[25] Bhimavarapu U, Chintalapudi N, Battineni G. Brain tumor detection and categorization with segmentation of improved unsupervised clustering approach and machine learning classifier. Bioengineering. 2024; 11(3):1-25.
[26] Zebari NA, Mohammed CN, Zebari DA, Mohammed MA, Zeebaree DQ, Marhoon HA, et al. A deep learning fusion model for accurate classification of brain tumours in magnetic resonance images. CAAI Transactions on Intelligence Technology. 2024; 9(4):790-804.
[27] Karimullah S, Wheeb AH, Shaik F. Detection and classification of brain tumor from MRI and CT images using harmony search optimization and deep learning. Journal of Artificial Intelligence Research & Advances. 2024; 11(3):31-49.
[28] Alqhtani SM, Soomro TA, Shah AA, Memon AA, Irfan M, Rahman S, et al. Improved brain tumor segmentation and classification in brain MRI with

FCM-SVM: a diagnostic approach. IEEE Access. 2024; 12:61312-35.
[29] Elgohr AT, Elhadidy MS, Elazab MA, Hegazii RA, El SMM. Multi-classification model for brain tumor early prediction based on deep learning techniques. Journal of Engineering Research. 2024; 8(3):1-9.
[30] Nassar SE, Yasser I, Amer HM, Mohamed MA. A robust MRI-based brain tumor classification via a hybrid deep learning technique. The Journal of Supercomputing. 2024; 80(2):2403-27.
[31] Alshuhail A, Thakur A, Chandramma R, Mahesh TR, Almusharraf A, Vinoth KV, et al. Refining neural network algorithms for accurate brain tumor classification in MRI imagery. BMC Medical Imaging. 2024; 24(1):1-20.
[32] Mathivanan SK, Sonaimuthu S, Murugesan S, Rajadurai H, Shivahare BD, Shah MA. Employing deep learning and transfer learning for accurate brain tumor detection. Scientific Reports. 2024; 14(1):1-15.
[33] Lakshmi K, Amaran S, Subbulakshmi G, Padmini S, Joshi GP, Cho W. Explainable artificial intelligence with UNet based segmentation and bayesian machine learning for classification of brain tumors using MRI images. Scientific Reports. 2025; 15(1):1-22.
[34] Nahiduzzaman M, Abdulrazak LF, Kibria HB, Khandakar A, Ayari MA, Ahamed MF, et al. A hybrid explainable model based on advanced machine learning and deep learning models for classifying brain tumors using MRI images. Scientific Reports. 2025; 15(1):1-21.
[35] Ilani MA, Shi D, Banad YM. T1-weighted MRI-based brain tumor classification using hybrid deep learning models. Scientific Reports. 2025; 15(1):1-16.

Dr. N. Kopperundevi is currently working as an Assistant Professor at Vellore Institute of Technology (VIT), Vellore. She completed her doctoral research in 2019 under Anna University, Chennai, specializing in Information and Communication Engineering. Her research interests include image processing, neural networks, fuzzy systems, machine learning, and deep learning. She has also guided more than fifteen undergraduate and postgraduate projects.
Email: kopperundevi.n@vit.ac.in

Ms. V. Lakshmi Praba is working as an Assistant Professor in the Department of Electronics and Communication Engineering at E.G.S. Pillay Engineering College. She completed her B.E. in Electronics and Communication Engineering and her M.E. in Communication Systems from the same institution. She has three years of teaching experience in engineering education.
Email: lakshmiprabavenkatesan@gmail.com

Dr. S. Senthilkumar is working as an Assistant Professor in the Department of Electronics and Communication Engineering at E.G.S. Pillay Engineering College, Nagapattinam. He completed his Ph.D. in Information and Communication Engineering at Anna University, Chennai, in 2023. He obtained his postgraduate degree in Nanoelectronics from SASTRA University, Thanjavur, and his undergraduate degree in Electronics and Communication Engineering from Anjalai Ammal Mahalingam Engineering College, Kovilvenni. He has more than twelve years of teaching experience.
Email: senthil.lanthiri@gmail.com

V. Mohan received his B.E. degree (1995) in Electrical and Electronics Engineering and his M.E. degree (2001) in Power Electronics and Drives from Bharathidasan University, Tiruchirappalli, India. He earned his Ph.D. in Electrical Engineering from Anna University, Chennai, India, in 2015. He has over twenty-five years of teaching experience and has contributed to more than forty publications in international journals and conference proceedings. His research interests include multilevel inverters, renewable energy systems, and drives and control.
Email: veerasamy.mohan@yahoo.com

Dhinesh Vijayakumar has over sixteen years of industry experience and currently serves as an Observability Architect and Data Engineering/Analytics Specialist at TMX Group, the parent organization of the Toronto Stock Exchange. His work focuses on enhancing application performance, availability, and data-driven intelligence across mission-critical financial systems.
Email: dhinesh.vijayakumar@tmx.com

Appendix I

S. No.	Abbreviation	Description
1	2D	Two-Dimensional
2	ACNN	Advanced Convolutional Neural Network
3	AFF	Adaptive Fuzzy Filtering
4	AHA	Artificial Hummingbird Algorithm
5	AI	Artificial Intelligence
6	BRANN	Bayesian Regularized Artificial Neural Network
7	BraTS	Brain Tumor Segmentation
8	CDBN	Convolutional Deep Belief Networks
9	CLAHE	Contrast-Limited Adaptive Histogram Equalization
10	CNN	Convolutional Neural Network
11	CSF	Cerebro Spinal Fluid
12	DLBTDC-CSO	Deep Learning-Based Brain Tumor Detection and Classification Using

		Chicken Swarm Optimization
13	FCM	Fuzzy C-Means
14	GAN	Generative Adversarial Network
15	GLCM	Grey-Level Co-Occurrence Matrix
16	GM	Gray Matter
17	GPU	Graphics Processing Unit
18	Grad-CAM	Gradient-Weighted Class Activation Mapping
19	HGG	High-Grade Gliomas
20	IDM	Inverted Difference Moment
21	IRMO	Improved Radial Movement Optimization
22	LGG	Lower Grade Glioma
23	LSTM	Long Short-Term Memory
24	MRI	Magnetic Resonance Imaging
25	PDSCNN	Parallel Depthwise Separable CNN
26	ReLU	Rectified Linear Unit
27	ResNet	Residual Neural Network
28	RRELM	Ridge Regression Extreme Learning Machine
29	SD	Standard Deviation
30	SVM	Support Vector Machine
31	WM	White Matter
32	XAISS-BMLBT	Explainable AI with Semantic Segmentation and Bayesian Machine Learning for Brain Tumors